

Synthesis and Structural Characterization of Se-Modified Carbon-Supported Ru Nanoparticles for the Oxygen Reduction Reaction

Vladimir I. Zaikovskii,[†] Kyatanahalli S. Nagabhushana,[‡] Vladimir V. Kriventsov,[†] Konstantin N. Loponov,[†] Svetlana V. Cherepanova,[†] Ren I. Kvon,[†] Helmut Bönnemann,^{*,‡,§} Dimitrii I. Kochubey,[†] and Elena R. Savinova^{*,†}

Boriskov Institute of Catalysis, Russian Academy of Sciences, Pr. Akademika Lavrentieva 5, 630090 Novosibirsk, Russia, Forschungszentrum Karlsruhe, ITC-CPV, Postfach 3640, D 76021, Germany, and Max-Planck-Institut für Kohlenforschung, Kaiser-Wilhelm-Platz-1, D 45470, Mülheim an der Ruhr, Germany

Received: November 20, 2005; In Final Form: January 24, 2006

This work is part of a continued research aimed at the understanding of the promoting role of Se in the enhancement of the electrocatalytic activity of Ru in the oxygen reduction reaction. The objective of this paper is to systematically investigate the transformation of Ru nanoparticles upon their modification with the increasing amounts of Se. The Se-modified Ru/C samples with Se:Ru ratio from 0 to 1 were prepared by reacting carbon-supported Ru nanoparticles with SeO₂ followed by reductive annealing and characterized using high-resolution transmission electron microscopy, energy-dispersive X-ray, X-ray diffraction analysis, X-ray photoelectron spectroscopy, and extended X-ray absorption fine structure. The results suggest that Se strongly interacts with Ru, resulting in the chemical bond between Ru and Se and formation of Ru selenide clusters whose core at low Se content can be described as Ru₂Se₂O_{0.5}. At Se:Ru = 1, high-resolution electron microscopy shows evidence of formation of core-shell particles, comprising a hexagonally packed Ru core and a Ru selenide shell with lamellar morphology. Modification of Ru nanoparticles with Se enhances their electrocatalytic activity in the oxygen reduction reaction, which is explained by the role of Se in inhibiting surface oxidation.

1. Introduction

Direct methanol fuel cells (DMFCs) have recently attracted considerable attention as alternative power sources for portable and vehicle applications (see, e.g., refs 1 and 2 and references therein). Their commercialization is, however, impeded by low efficiencies and high costs. Methanol crossover through the polymer membrane from the anode to the cathode compartment with concomitant depolarization of the Pt cathode is one of the reasons for the yet insufficient performances of DMFCs.¹ Development of active and highly selective oxygen reduction reaction (ORR) catalysts has remained a challenge stimulating research in the area of methanol-tolerant cathode materials.

Ruthenium-based cluster compounds containing selenium (Ru_xSe_y, Mo_zRu_xSe_y) have been proposed as ORR catalysts by Alonso-Vante et al.^{3–6} These materials were synthesized by thermolysis of triruthenium dodecacarbonyl in organic solvents in the presence of selenium. Electrochemical investigations using rotating ring-disk have proven that oxygen reduction occurs predominantly via a 4e[−] path, with the amount of hydrogen peroxide produced not exceeding 6%.^{5,7} The presence of Se strongly enhances the catalytic activity of Ru toward ORR. Particular interest in these compounds resides in their methanol tolerance, which makes them promising for DMFC applications. In situ EXAFS investigations on a series of chalcogene-doped Ru clusters^{8,9} have proven that during the electrocatalytic process

oxygen binds to Ru sites. Despite numerous investigations on the structure and electrochemical properties of Ru_xSe_y cluster materials,^{4,5,10–12} the role of Se in the enhancement of the catalytic activity is not fully understood yet. Recent studies have shown that similar ORR enhancement can be reached by modifying Ru nanoparticles with Se.^{13,14} Fundamental understanding of the role of Se in the enhancement of Ru catalytic activity is needed for designing active and methanol tolerant ORR catalysts based on carbon-supported Ru_xSe_y clusters.

The objective of this paper is to systematically investigate the transformation of Ru nanoparticles upon their modification with increasing amounts of Se and explore concomitant changes in the catalytic activity in the ORR. We believe that this work may be of interest to a broad audience since it explores a particular case of tailoring metal nanoparticles via their surface modification as a means to influence their structure, electronic properties, and catalytic activities.

2. Experimental Section

2.1. Catalyst Preparation. 2.1.1. Preparation of 20 wt % Ru on Vulcan XC 72. The synthesis of 20 wt % Ru/C was carried out under argon using dry solvents. Anhydrous RuCl₃ was procured from Acros and was used as received. In a 2-L two-neck flask fitted with a dropping funnel and a vacuum adapter, maintained under a steady flow of argon, 2.868 g (13.8 mmol) of anhydrous ruthenium chloride and 1 L of dry THF were introduced and sonicated for 15 min to generate a uniform suspension of the salt. To this suspension, 5.6 g of Vulcan XC 72 was introduced, and the mixture was stirred vigorously for 2 h at room temperature. At the end of this time the flask was

* Corresponding authors: Helmut Bönnemann (boennemann@mpi-muelheim.mpg.de) and Elena R. Savinova (elensav@catalysis.ru).

[†] Boriskov Institute of Catalysis, Russian Academy of Sciences.

[‡] Forschungszentrum Karlsruhe.

[§] Max-Planck-Institut für Kohlenforschung.

TABLE 1: Sample Description

no.	description	Se:Ru (atomic ratio)	abbreviation
1	20 wt % Ru	0	Ru/C
2	17.3 wt % Ru + 13.5 wt % Se	1.0	Ru ₁ Se ₁ /C
3	18.3 wt % Ru + 8.5 wt % Se	0.59	Ru ₁ Se _{0.59} /C
4	19.7 wt % Ru + 4.5 wt % Se	0.30	Ru ₁ Se _{0.3} /C
5	19.6 wt % Ru + 2.2 wt % Se	0.146	Ru ₁ Se _{0.15} /C

placed in an oil bath maintained at 50 °C, 27.0 mL of 1.5 M LiBet₃H/THF solution was dripped over 2 h, and the resulting mass was allowed to stir vigorously overnight at 50 °C. Then the stirring was stopped, and the flask was allowed to cool to room temperature. Colorless and clear supernatant was pressed off and the precipitate was washed two times with 150 mL portions of THF and dried. The residue, which is a free flowing mass, was conditioned¹⁵ at 200 °C using argon (5 min) followed by hydrogen (30 min) and again argon (5 min). The sample tube was allowed to cool to room temperature and the sample downloaded. This enabled stable, 20 wt % Ru/C catalyst, and the yield was 7.01 g.

2.1.2. Modification of Ru/C with Se. Various amounts of H₂SeO₃ (SeO₂ in water) were added to 20 wt % Ru/C sample in order to produce Se-modified samples with different Se/Ru ratios. The sample descriptions are given in Table 1. The preparation was performed as described below. A stock solution of 1.0 g of SeO₂ in 100 mL of THF and water (1:1 v/v) was initially prepared. To produce RuSe(1:1)/Vulcan sample, 22 mL from this solution was added to 1.0 g of 20 wt % Ru/Vulcan suspended in 50 mL of THF, the whole mass was stirred for 2 h at room temperature, and the solvent was evaporated at reduced pressures. The resulting free flowing mass was then transferred into a conditioning apparatus and reductively annealed at 200 °C (using Ar for 5 min followed by H₂ for 1 h and then by Ar for 5 min). This generated (17.3 wt % Ru + 13.5 wt % Se)/Vulcan XC-72 catalyst with Se:Ru = 1:1 (a/o). Similarly, using 13.0, 6.6, and 3.2 mL of SeO₂ solution, catalysts with Se content of 8.5, 4.5, and 2.2 wt % were prepared (Table 1).

2.2. Sample Characterization. X-ray diffraction patterns were obtained using an X-ray diffractometer (Siemens, Cu K α radiation) featuring a homemade gastight high-temperature camera reactor.¹⁶ A catalyst sample taken from air was rereduced in H₂ flow at 150 °C for 1 h and then cooled to room temperature, then its X-ray diffraction pattern was recorded by scanning in the 2 θ angle range from 10° to 100°. Calculation of the lattice constants and the average size of metal crystallites were based on the angle position and on the full width at half-maximum (fwhm) of the peaks, respectively. The values of the lattice constants were determined by means of the least-squares method. The average sizes of metal crystallites were calculated using a Scherrer formula from a fwhm of 110 diffraction line, which for all samples does not overlap with other lines.

The X-ray photoelectron spectroscopy (XPS) measurements were taken with VG ESCALAB HP (Thermo VG Scientific) photoelectron spectrometer using Al K α excitation and constant pass energy (Ag 3d_{5/2} fwhm = 1.2 eV) operated under the base pressure of $\leq 2 \times 10^{-9}$ mbar. The spectra were referenced to Cu 2p_{3/2} (932.7 eV), Ag 3d_{5/2} (368.2 eV), and Au 4f_{7/2} (84.0 eV) lines. The powder samples were mounted onto the holder using the conductive double-side adhesive tape, 3M. Due to the conductive nature of the samples, charging effects were not observed. All experimental XPS data were processed using XPS PEAK software Version 4.1.¹⁷ Ru 3d + C 1s spectra were

deconvoluted using the peak parameters obtained from the Ru 3d peak for polycrystalline Ru sample recorded at the same XPS machine.

HRTEM (high-resolution transmission electron microscopy) micrographs were obtained with a JEM-2010 instrument with lattice resolution 1.4 Å and accelerating voltage 200 kV. Periodic images of lattice structures in electron micrographs were analyzed using digital Fourier transformation. Local elemental analysis was performed with the energy dispersive X-ray (EDX) method on the energy-dispersive X-ray Phoenix spectrometer equipped with Si (Li) detector with energy resolution not worse than 130 eV. Samples for the electron microscopy were fixed on “holey” carbon films supported on copper grids.

The extended X-ray absorption fine structure (EXAFS) spectra of the Se–K and Ru–K edges for all the samples studied were obtained at the EXAFS Station of the Siberian Synchrotron Radiation Center. The storage ring VEPP-3 with an electron beam energy of 2 GeV and the average stored current of 90 mA was used as the radiation source. The X-ray energy was monitored with a channel cut Si(111) monochromator. Spectra were recorded under the transmission mode using two ionization chambers as detectors.

The EXAFS spectra were treated using the standard procedure^{18,19} by “Viper” code.^{20,21} The background was removed by extrapolating the preedge region onto the EXAFS region by Victoreen’s polynomials. Three cubic splines were used to simulate the smooth part of the absorption coefficient. The inflection point of the edge of the X-ray absorption spectrum was used as the initial point ($k = 0$) of the EXAFS spectrum. The radial distribution function (RDF) was calculated from the EXAFS spectra in $k\chi(k)$ as the modulus of the Fourier transform in the wavenumber intervals 3.3–11.5 Å⁻¹ and 3.3–12.5 Å⁻¹ for Se–K and Ru–K edges, respectively. Curve fitting procedure with EXCURV92²² code was employed to determine the distances and the coordination numbers in similar wavenumber intervals after preliminary Fourier filtering using known X-ray diffraction (XRD) data for the bulk compounds. Debye–Waller factors were fixed at 0.005 Å².

2.3. Electrochemical Measurements. Electrolyte solutions were prepared from Milli-Q water (18 M Ω ·cm) and H₂SO₄ (Suprapur, Merck or suprapure, Russia). Working electrodes were prepared by pipetting an aliquot of aqueous suspension containing 1.5 mg mL⁻¹ of Ru_xSe_y/Vulcan sample either on the polycrystalline gold foil (cleaned with aqua regia and annealed in the hydrogen flame) or on the glassy carbon (GC) rod (polished to a mirror finish and cleaned in the ultrasonic bath in ethanol, acetone, and water) and drying under the Ar flow. The resulting films were mechanically stable and showed reproducible cyclic voltammograms (CVs). For ORR experiments Nafion was added to the catalyst suspension to produce 10 wt % loading in order to improve the particle distribution on the GC support. After each experiment Ru_xSe_y/Vulcan was removed from the substrate by wiping the surface under a water flow. Electrochemical measurements were carried out in a three-electrode cell at 298 K in an Ar (for CV) or O₂ (for ORR) atmosphere. The counter electrode was Pt foil, and the reference electrode was mercury sulfate electrode (MSE) Hg/Hg₂SO₄/0.1 M H₂SO₄ connected to the working electrode compartment via Luggin capillary. Potentials were controlled using an Autolab PGSTAT30 potentiostat and are quoted vs reversible hydrogen electrode RHE ($E_{\text{MSE}} = 0.73$ V vs RHE).

3. Results and Discussion

3.1. X-ray Diffraction. Figure 1a shows diffractograms of 20% Ru/Vulcan (no Se) stored in air (black) and after its

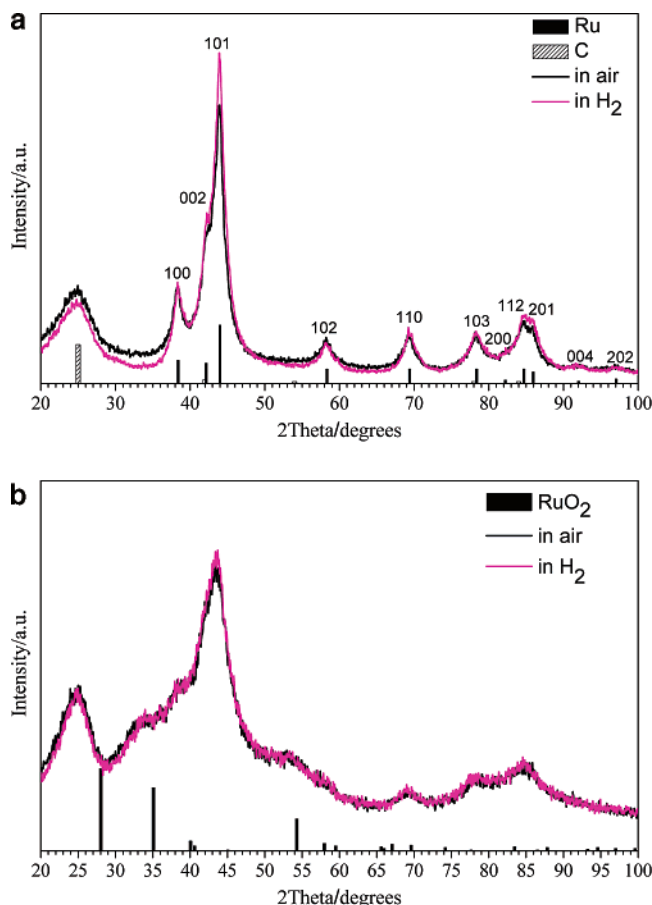


Figure 1. XRD patterns for (a) Ru/C and (b) Ru₁Se₁/C stored in air (black) and in hydrogen atmosphere after 1 h of reduction at 150 °C (pink).

reduction in hydrogen atmosphere for 1 h at 150 °C (pink). Both samples show characteristic reflections of hexagonally packed metallic ruthenium. The sample treated in H₂ at 150 °C shows higher intensities of the reflections corresponding to metallic Ru (most noticeable is the increase of the reflection from (101) plane) and the decrease of the background in 2θ interval from 28° to 38°. Treatment in hydrogen at 200 °C gives the same result. Obviously, under ambient conditions Ru nanoparticles are partially oxidized (supposedly to RuO₂) but reduced when heated in hydrogen. Comparison of the XRD patterns for Se containing samples under the ambient atmosphere and after their reduction in hydrogen shows that the higher the amount of Se, the smaller the contribution of reducible components to the diffractogram and, hence, the lower the amount of Ru oxides in the samples. Figure 1b shows that, e.g., for the Ru₁Se₁/C sample the diffractograms before and after the hydrogen treatment overlap. We thus conclude that Se protects Ru particles from the oxidation. This is in agreement with Dassenoy et al.¹¹ who used X-ray diffraction at wide angles to prove that coordination of selenium results in the chemical stabilization of Ru clusters against oxidation. Further on we will discuss and compare the diffractograms for reduced Ru/C and Ru_xSe_y/C samples.

The average particle size of Ru nanoparticles in 20% Ru/Vulcan estimated from the 110 diffraction line equals 5.5 nm (Table 2). Addition of increasing amounts of Se to the samples results in remarkable and systematic changes in the XRD patterns (Figure 2), which show up in the (i) decrease of the intensities of Ru metal reflexes and their broadening, (ii) shift of Ru(101) diffraction peak to smaller angles, (iii) increase of

TABLE 2: Structural Parameters Obtained from XRD Data

sample	$\langle D \rangle$, ^a nm	a , ^b Å	c , ^b Å
Ru/C	5.5	2.708(1)	4.288(1)
Ru ₁ Se _{0.15} /C	4.0	2.709(1)	4.302(3)
Ru ₁ Se _{0.3} /C	4.0	2.710(2)	4.307(4)
Ru ₁ Se _{0.59} /C	3.5	2.716(8)	4.282(14)
Ru ₁ Se ₁ /C	~3		
Ru metal (JCPDS card #06-0663)		2.705	4.281

^a Average particle size for metallic Ru phase. ^b Lattice parameters for metallic Ru phase.

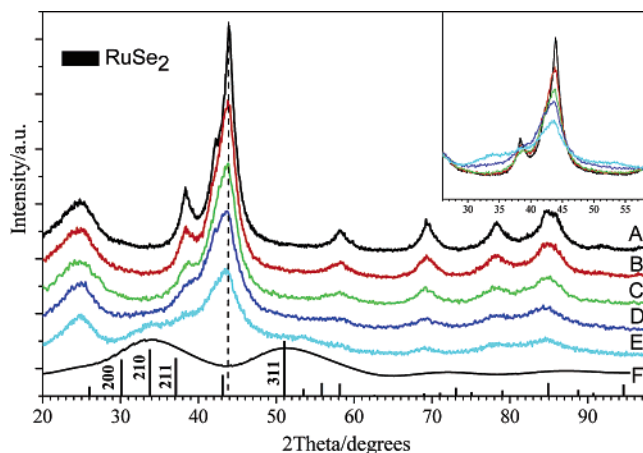


Figure 2. XRD patterns acquired after 1 h of reduction at 150 °C in the hydrogen atmosphere for Ru/C (A), Ru₁Se_{0.15}/C (B), Ru₁Se_{0.3}/C (C), Ru₁Se_{0.59}/C (D), and Ru₁Se₁/C (E). F corresponds to the diffraction pattern for RuSe₂ with the crystal size 10 Å × 10 Å × 11.86 Å simulated using the program described in ref 26. The insert shows selected 2θ interval.

the intensity in 2θ intervals from 28° to 38° and from 48° to 56° (see insert in Figure 2). The above changes point to the decrease of the size of Ru crystallites from 5.5 nm down to ca. 3 nm (Table 2) and to a partial transformation of Ru metal into another compound. This new compound is highly dispersed (coherent scattering domain estimated using the Scherrer formula is ca. 0.6–0.9 nm). Considering the stability of this compound in a hydrogen atmosphere at 200 °C, we conclude that it cannot correspond to RuO₂ despite the fact that it shows reflections in the same 2θ intervals.

To account for the transformation of diffraction patterns upon Se addition, we refer to the literature data. Ru is known to form a variety of organometallic selenide cluster compounds with M₂Se₂, M₃Se, M₃Se₂, and M₄Se₂ cores (see ref 23 and references therein) but only one inorganic selenide RuSe₂ which adopts a cubic pyrite (FeS₂) structure.^{24,25} This is at variance with other noble (e.g., Pd²⁵) or transition metals (e.g., Fe), which form a wide variety of chalcogenides of different stoichiometry. We have simulated the diffraction pattern for highly dispersed RuSe₂ with the crystal size 10 Å × 10 Å × 11.86 Å (two unit cells) using the program described in ref 26. The program allows simulation of diffraction patterns for crystallites of a given size. It takes into account the size confinement and some details of microstructure. The simulated diffraction pattern is plotted in Figure 2. The positions of diffraction lines for the simulated diffractogram are in agreement with those observed in the experiment. Hence, XRD data are in favor of formation of RuSe₂. However, given the broadness of the reflections, we consider this observation insufficient to unambiguously prove formation of RuSe₂.

3.2. Electron Microscopy. Figure 3a shows transmission electron micrograph of 20% Ru/Vulcan. Ru nanoparticles are well dispersed and distributed over the carbon surface. The average d_N , the surface average d_s , and the mass average d_m particle sizes were calculated from the size distribution (see inset to Figure 3a) as follows

$$d_N = \sum_i N_i d_i / \sum_i N_i = 3.9 \text{ nm}$$

$$d_s = \sum_i N_i d_i^3 / \sum_i N_i d_i^2 = 5.0 \text{ nm}$$

$$d_m = \sum_i N_i d_i^4 / \sum_i N_i d_i^3 = 5.7 \text{ nm}$$

The latter is in very good agreement with the average particle size estimated from XRD data. Since XRD probes the bulk, it gives an estimate of the mass average particle size. Modification of 20% Ru/Vulcan with Se alters its morphology, leading to the decrease in the size of Ru nanocrystals and their partial agglomeration (Figure 3b,c). Because of the particle agglomeration we were not able to build particle size distributions and calculate the average particle size for Se-containing samples.

At high Se loadings (Se:Ru = 1), TEM images provide evidence of formation of core-shell or so-called yolk-shell particles (Figure 4c). As confirmed by the lattice spacing, the core (the yolk) of these particles is composed of hexagonally packed Ru metal. The results of the integral EDX analysis are in agreement with the nominal composition of the catalysts. Selected area elemental analysis of the sample areas containing Ru particles proves that Se is deposited exclusively on Ru. Hence, particle shells must contain Se. High-resolution TEM images reveal periodic lattice along the layer covering Ru particles (the insert in Figure 4c). The lattice spacing equals 2.7 Å, which coincides with the d_{012} spacing for RuSe₂ phase. However, bulk RuSe₂ adopts cubic pyrite structure while the shells around Ru nanoparticles clearly show lamellar morphology with the interlayer spacing of ca. 6–7 Å. Lamellar structures have been reported for chalcogenides of Mo (MoS₂ and MoSe₂), Fe (FeS), and some noble metals, but not for Ru.²⁵ It is thus likely that in this work we observe yet unknown lamellar Ru_xSe_y forming shells around hexagonally packed Ru cores. This structure is very stable and does not decompose under the high-energy electron beam of the electron microscope. The reason the thin layer of Ru_xSe_y adopts a structure different from bulk RuSe₂ is being explored²⁷ and may be related to the size confinement. Elementary Se adopts a variety of crystalline (and amorphous) modifications, including lamellar structures. However, the shell consisting of elementary Se is highly unlikely in view of the chemical bond formation between Ru and Se proven by XPS and EXAFS data (see sections 3.3. and 3.4)

It is interesting to mention that along with the core-shell particles hollow structures are occasionally found in Ru₁Se₁/C. Their outer layer adopts the same structure as the shell of core-shell particles, but the core is hollow. Yin et al.²⁸ have recently reported formation of hollow cobalt selenide (sulfide) nanocrystals through the interaction of Co nanocrystals with either Se or S. This phenomenon has been explained by the Kirkendall effect in which pores form because of the difference in the diffusion rates between two components in a diffusion couple. Higher outward diffusion of the metal atoms/ions vs inward diffusion of selenium or sulfur was invoked to explain the structures formed.

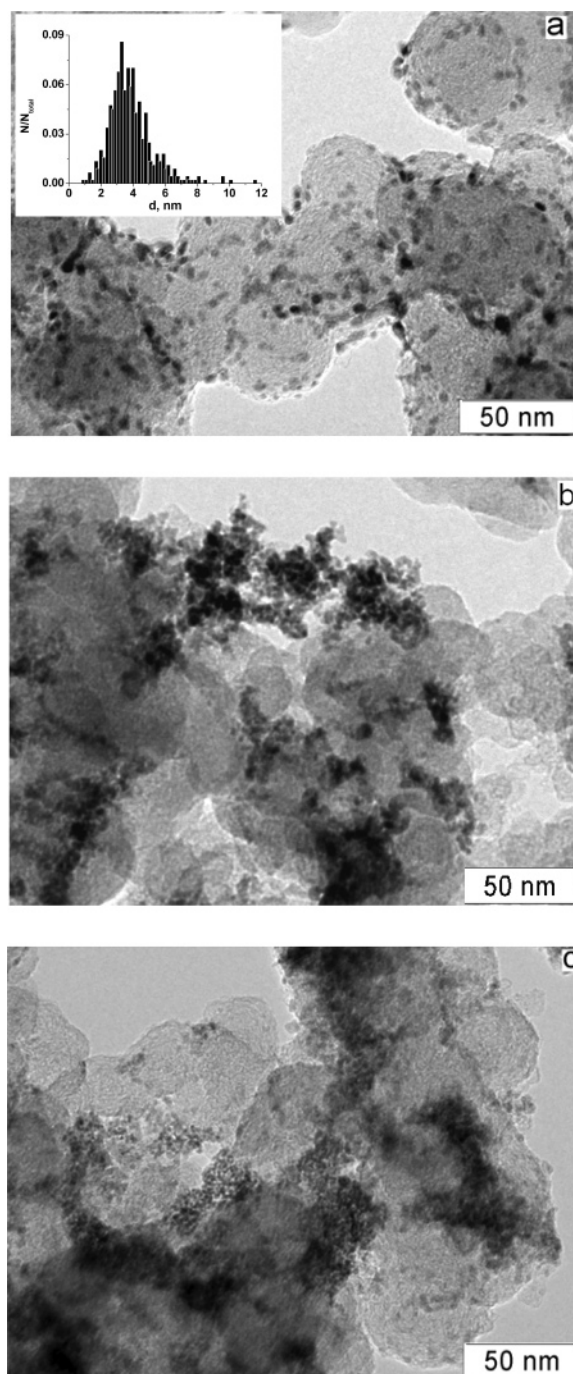


Figure 3. TEM images of Ru/C (a), Ru₁Se_{0.15}/C (b), and Ru₁Se₁/C (c). The insert in Figure 3a shows the particle size distribution.

At Se/Ru < 1 we observed clusters on Ru nanoparticles and only occasionally core-shell particles and hollow structures. Figure 4b represents a typical HRTEM image for a Ru₁Se_{0.15}/C sample. These clusters might have been attributed to Ru oxides (cf. Figure 3 top and middle), if it were not in conflict with XRD results (see above). Hence, we tentatively attribute these clusters also to Ru_xSe_y.

3.3. X-ray Photoelectron Spectroscopy. The survey XPS spectrum of pristine Vulcan XC-72 reveals C, O, and trace quantities of Si and S, which are normally found in carbon blacks as impurities. For Ru/C and Ru_xSe_y/C samples the spectra of C 1s, O 1s, Se 3d, Ru 3d, and Ru 3p regions were acquired; the latter was recorded for the quantitative analysis because the Ru 3d line partially overlaps with the C 1s peak. The XPS analyses reveal that Ru deposition on Vulcan XC-72 does not

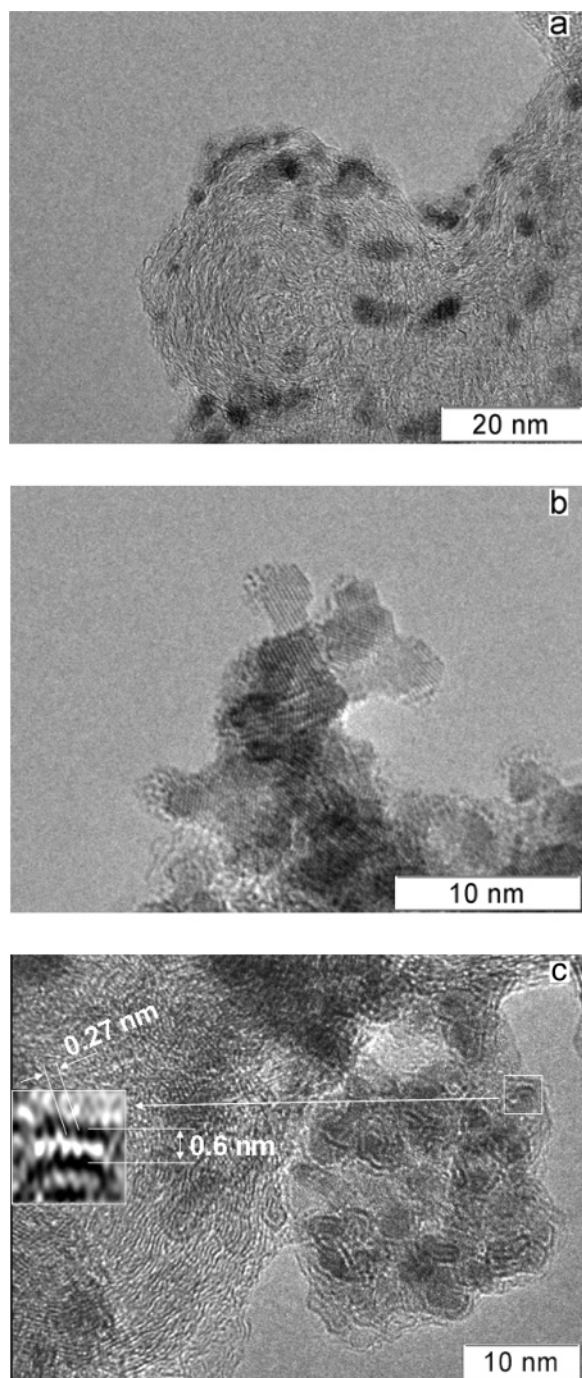


Figure 4. HRTEM images of Ru/C (a), $\text{Ru}_1\text{Se}_{0.15}/\text{C}$ (b), and $\text{Ru}_1\text{Se}_1/\text{C}$ (c). The insert in Figure 4c shows the Fourier filtered image of the fragment of core-shell particle.

influence the C 1s peak position at 284.4 eV but results in the alteration of the O 1s signal and the introduction of a small amount of chlorine ($\text{Cl}/\text{C} = 0.007$). The latter obviously results from the catalyst synthesis (see Experimental Section). An inspection of the O 1s spectral region (Figure 5a) indicates that after the deposition of ruthenium two new oxygen states appear on the surface, with O 1s binding energy (BE) of 531.6 eV (curve D) and 529.9 eV (curve C in Figure 5a). The intensity of the latter correlates with the intensity of the peak located at 281.5 eV in Ru 3d_{5/2} spectral region (Table 3) and can thus be attributed to the oxygen in Ru(IV) oxide(s). This is in agreement with the XRD data that also gives evidence for the partial oxidation of Ru particles. Note that samples were stored under the ambient conditions and were not subjected to any pretreat-

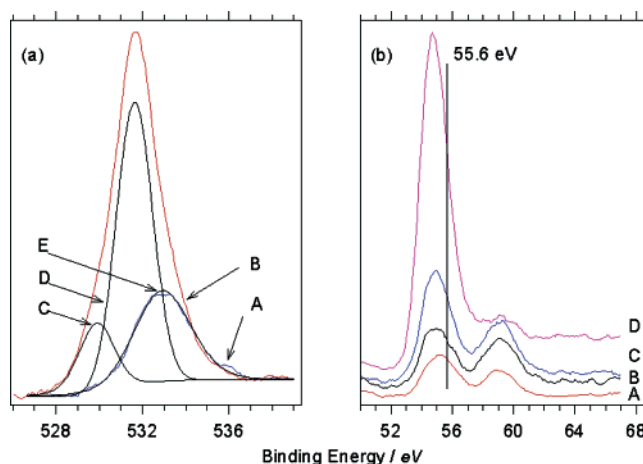


Figure 5. (a) O 1s region for pristine Vulcan XC-72 (curve A) and Ru/C (curve B) and the deconvolution of spectrum B: see text for details. (b) Se 3d spectra for $\text{Ru}_1\text{Se}_{0.15}/\text{C}$ (A), $\text{Ru}_1\text{Se}_{0.3}/\text{C}$ (B), $\text{Ru}_1\text{Se}_{0.59}/\text{C}$ (C), and $\text{Ru}_1\text{Se}_1/\text{C}$ (D). The line marks the position of Se 3d_{5/2} peak for elemental selenium.

ment in the ultrahigh vacuum (UHV) chamber. The quantitative analysis of the Ru 3p region indicates that the $\text{Ru}^{4+}/\text{Ru}_{\text{total}}$ ratio amounts to 0.26. O 1s with 531.6 eV BE can be tentatively attributed to the oxygen-containing groups²⁹ on the surface of carbon support, which may be introduced during the catalyst synthesis. The Ru/C atomic ratio calculated from the intensities of Ru 3d (Ru 3p) and C 1s lines (Table 3) is in agreement with the atomic ratio for 20% Ru/Vulcan (0.030) estimated without considering the self-screening effect. In practice of XPS this means that Ru particles are small enough to avoid significant intensity losses through self-screening and are “homogeneously” distributed over the support surface. This result is in agreement with the TEM data.

Addition of selenium to Ru/C leads to the following transformations. First, the $\text{Ru(IV)}/\text{Ru}(\text{total})$ ratio continuously decreases from 0.26 for Ru/C to 0.16 for $\text{Ru}_1\text{Se}_1/\text{C}$. Second, the Ru signal intensity drops significantly. A number of possible explanations can be suggested in order to account for the experimentally observed attenuation of Ru/C atomic ratio: (i) decrease of the Ru amount on the support due to its washing out; (ii) enlargement of Ru particles (due to their sintering or agglomeration) so that self-screening effect becomes significant; (iii) encapsulation of Ru particles by another elements/species; and (iv) chemical compound formation. Decrease in the amount of Ru during Se deposition can be ruled out since no washing is involved in this particular synthetic step and the conditioning step that follows (see 2.1.2). Agglomeration of Ru nanoparticles indeed takes place (see 3.2) but cannot fully explain the experimentally observed decrease of Ru signal intensity (see TEM data). Before discriminating between (iii) and (iv) let us examine the Se 3d_{5/2} region (Figure 5b). According to ref 30, the Se 3d line consists of two peaks separated by 0.86 eV, although the achieved spectrometer resolution was not sufficient to resolve them. Deconvolution of the Se 3d_{5/2} region (not shown) using XPS Peak software reveals at least two different states of Se in the samples. The doublet at 54.4 and 55.3 eV can be attributed to Ru selenide. Similar values were reported by Alonso-Vante et al. for molybdenum-doped Ru selenide.³¹ The intensity of the selenide peak increases along with the increase in Se concentration, so that at high Se loads it gives the predominant contribution. The second doublet comprises two peaks at 58.7 and 59.6 eV, which are characteristic of Se oxides, e.g., SeO_2 ; its intensity is practically independent of the

TABLE 3: Binding Energies (BE) and Atomic Ratios of the Elements (AR^a) Calculated from XPS Data

element		sample					
		Vulcan XC-72	Ru/C	Ru ₁ Se _{0.15} /C	Ru ₁ Se _{0.3} /C	Ru ₁ Se _{0.59} /C	Ru ₁ Se ₁ /C
O 1s	AR	0.045	0.148	0.076	0.097	0.055	0.086
Ru 3d _{5/2}	BE(Ru ⁰)		280.4	280.3	280.3	280.4	280.3
	AR (Ru ⁰) ^b		0.019	0.0104	0.0095	0.0088	0.016
	BE(Ru ⁴⁺)		281.5	281.4	281.4	281.5	281.4
	AR(Ru ⁴⁺) ^b		0.0068	0.0036	0.0025	0.0022	0.0030
	AR(Ru _{total}) ^b		0.026	0.014	0.012	0.011	0.019
Ru 3p	AR(Ru _{total}) ^b		0.030	0.015	0.013	0.013	0.020
Se 3d _{5/2}	BE(Se ⁴⁺)			58.7	58.8	58.7	58.7
	AR(Se ⁴⁺) ^b			0.0009	0.0022	0.0026	0.0019
	BE(Se ⁰)			55.6	55.6	55.6	55.6
	AR(Se ⁰) ^b			0.0009	0.0008	0.0012	0.0028
	BE(Se ²⁻)			54.4	54.4	54.4	54.4
	AR(Se ²⁻) ^b			0.0014	0.0016	0.0034	0.0148
	AR(Se _{total}) ^b			0.0032	0.0046	0.0072	0.0195
	AR(Se _{total}) ^c			0.0043	0.0090	0.0179	0.0297
Se/Ru ^b	AR			0.21	0.35	0.55	0.97
Se/Ru ^c	AR			0.146	0.30	0.59	1

^a Atomic ratio (AR) is related to carbon (if not otherwise stated). ^b Calculated from XPS data. ^c Calculated from the nominal sample composition.

Se content. The presence of some amount of elemental Se (the first line of the doublet located at 55.6 eV³⁰) cannot be excluded either; its maximum contribution has been estimated and is tabulated in Table 3. The total concentration of Se calculated from the XPS data is lower than expected from its load and gives evidence of inhomogeneous distribution of Se on the surface. Meanwhile, the measured Se/Ru ratios agree very well with the calculated ones (Table 3).

The XPS data on the BE and elemental concentrations corroborate that Se interacts with Ru forming ruthenium selenide. Unfortunately, its exact stoichiometry cannot be determined from the XPS data alone because of the coexistence of Ru selenide and metallic Ru. The latter is confirmed by TEM and XRD. Considering the screening of Ru signal, we conclude that Ru selenide is located on the surface of Ru particles (Ru particles are “encapsulated” by the selenide layer at high Se contents and are covered by Ru selenide clusters at low Se contents). The latter inhibits Ru oxidation under the ambient conditions. Note that the redistribution of Ru particles on the support surface and their agglomeration, which are probably stimulated by the formation of Ru selenide, may also contribute to the divergence between the experimental and calculated atomic compositions. Obviously, some amount of Se is present in the oxidized form. This will be further discussed in section 3.4.

3.4. EXAFS. Figure 6 represents the radial distribution functions (RDFs) obtained via Fourier transformation of the EXAFS spectra taken at the Ru K-edge. The RDF for Ru/C shows a peak corresponding to Ru–Ru interactions, a peak due to Ru–O interactions, and a few maxima at longer distances also corresponding to Ru–Ru in the higher shells (see results of the fitting below). Addition of the increasing amounts of Se results in the (i) strong attenuation of the maximum corresponding to Ru–Ru distance in the first coordination shell, (ii) decrease in the intensities of the peaks corresponding to Ru–Ru distances in higher shells, and (iii) significant changes in the range of short distances ($R - \delta_i \sim 1.7\text{--}2.2$ Å). The EXAFS data on the interatomic distances and coordination numbers describing Ru local coordinations obtained through fitting the EXAFS spectra are represented in Table 4.

Let us first concentrate on the EXAFS data for pristine Ru/C sample. The major part of ruthenium is present in metallic phase. This is proved unambiguously by the comparison of the

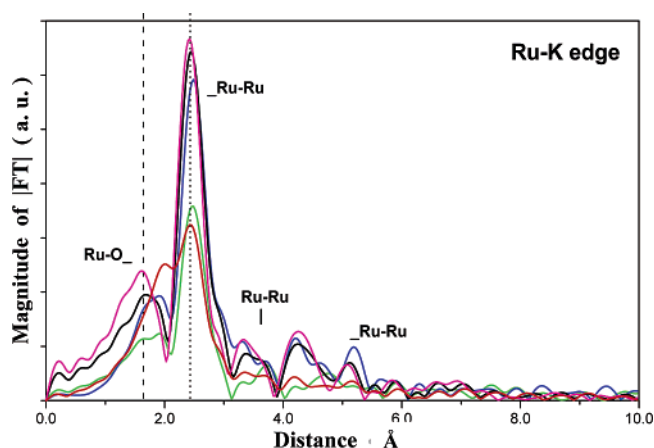


Figure 6. Radial distribution functions obtained via Fourier transformation of k^1 -weighted $\chi(k)$ for Ru K-edge for Ru/C (pink), Ru₁Se_{0.15}/C (black), Ru₁Se_{0.3}/C (blue), Ru₁Se_{0.59}/C (green), and Ru₁Se₁/C (red). The distance corresponds to $R - \delta_i$, where δ_i is the phase shift and depends on the type of the atom.

calculated set of Ru–Ru distances and coordination numbers (Table 4) with those for the metallic Ru reference.³² Somewhat lower coordination numbers (in comparison to the Ru⁰ reference) may be explained by the small particle size (5.5 nm) and some distortions caused by the presence of surface oxides. Along with Ru⁰ some amount of Ru is present in the oxidized form. The calculated Ru–O distances are close to those for the bulk ruthenium oxide (RuO₂, ref 33). However, the Ru–Ru distance at ~ 3.1 Å characteristic of Ru–O–Ru in bulk RuO₂ is not observed ($N = 0.1$ tabulated in Table 4 is at the detection limit of the method). Hence, bulk ruthenium dioxide is rather unlikely and we infer formation of surface Ru oxide.

We now move to the discussion of the structural changes induced by the addition of Se. As the amount of Se increases, the Ru–Ru coordination numbers decrease systematically and for Ru₁Se₁/C they drop by ca. a factor of 2 compared to the pristine Ru/C. This can be attributed to (i) the decrease in the size of Ru nanoparticles (cf. XRD and TEM data) and (ii) their distortion due to the interaction with Se. Significant changes are observed also at shorter distances and are manifested by the diminution of the amplitude of the peak and the shift to longer distances. The fitting indicates (Table 4) that Ru–O

TABLE 4: Distances (R) and Coordination Numbers (N) for $\text{Ru}_x\text{Se}_y/\text{C}$ Samples (as calculated from Ru K-edge EXAFS spectra) and for Reference Compounds^a

	Ru/C		$\text{Ru}_1\text{Se}_{0.15}/\text{C}$		$\text{Ru}_1\text{Se}_{0.3}/\text{C}$		$\text{Ru}_1\text{Se}_{0.59}/\text{C}$		$\text{Ru}_1\text{Se}_1/\text{C}$		RuO_2^{33}		Ru^0^{32}		$\text{Cs}_2\text{RuO}_4^{52}$		RuSe_2^{24}	
	$R, \text{\AA}$	N	$R, \text{\AA}$	N	$R, \text{\AA}$	N	$R, \text{\AA}$	N	$R, \text{\AA}$	N	$R, \text{\AA}$	N	$R, \text{\AA}$	N	$R, \text{\AA}$	N	$R, \text{\AA}$	N
Ru—O															1.75	1		
Ru—O	1.92	0.9	1.92	0.6	1.93	0.5	1.93	0.4	1.95	0.4	1.92	2			1.76	2		
Ru—O	2.05	1.6	2.05	1.2	2.06	0.8	2.07	0.5			2.00	4			1.77	1		
Ru—Se	-								2.44	1.2							2.45	6
Ru—Se																	3.81	6
Ru—Se																	3.92	2
Ru—Se																	4.87	6
Ru—Ru	2.63	4.8	2.63	4.6	2.62	4.0	2.63	2.8	2.64	2.5	3.11	2	2.65	6	5.36	2		
Ru—Ru	2.73	5.1	2.73	5.1	2.73	5.0	2.73	2.9	2.74	2.8	3.54	8	2.71	6	5.78	2		
Ru—Ru	~ 3.10	~ 0.1	~ 3.10	~ 0.0	~ 3.10	~ 0.0	~ 3.10	~ 0.0	~ 3.10	~ 0.0	4.49	4	3.79	6	5.96	2		
Ru—Ru	3.77	3.2	3.77	2.6	3.78	2.2	3.79	1.6	3.76	1.5								
Ru—Ru	4.27	0.9	4.27	0.8	4.26	0.7	4.26	0.4	4.27	0.5	5.46	8	4.28	2	3.75–4.00 ^b	7 ^b		
Ru—Ru	4.65	6.2	4.65	5.1	4.67	4.9	4.68	1.6	4.66	1.5	5.64	8	~ 4.67	18	4.74–4.85 ^b	4 ^b		

^a The values of Debye–Waller factors are fixed at 0.005 \AA^2 . ^b Ru–Cs.

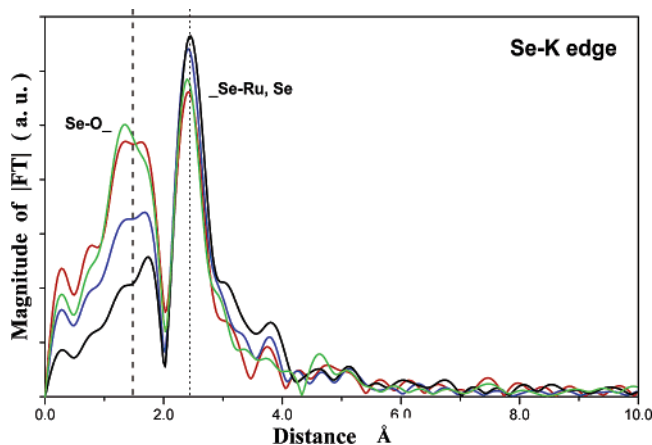


Figure 7. Radial distribution functions obtained via Fourier transformation of k^1 -weighted $\chi(k)$ for Se K-edge for $\text{Ru}_1\text{Se}_{0.15}/\text{C}$ (black), $\text{Ru}_1\text{Se}_{0.3}/\text{C}$ (blue), $\text{Ru}_1\text{Se}_{0.59}/\text{C}$ (green), and $\text{Ru}_1\text{Se}_1/\text{C}$ (red). The distance corresponds to $R - \delta_i$.

coordination numbers diminish systematically in the sequence: $\text{Ru}/\text{C} > \text{Ru}_1\text{Se}_{0.15}/\text{C} > \text{Ru}_1\text{Se}_{0.3}/\text{C} > \text{Ru}_1\text{Se}_{0.59}/\text{C}$, and for $\text{Ru}_1\text{Se}_1/\text{C}$ the RDF can only be fitted by considering a Ru–Se neighbor with a coordination distance of 2.44 \AA and coordination number of 1.2. For samples with $\text{Se}/\text{Ru} < 1$, Ru–Se average coordination numbers are small and fitting must consider both O and Se neighbors. This is, however, not possible because of the limitation of the number of the independent fitting parameters. As discussed above, Ru is known to form diselenide (RuSe_2) with pyrite structure^{24,25} and a variety of organometallic selenide cluster compounds with M_2Se_2 ,³⁴ M_3Se , M_3Se_2 ,³⁵ and M_4Se_2 cores. The Ru–Se distance in inorganic Ru diselenide is 2.45 \AA ;²⁴ similar distances are observed in organometallic Ru_xSe_y complexes.

To learn more about Se bonding in $\text{Ru}_x\text{Se}_y/\text{C}$ samples, EXAFS spectra at the Se K-edge were taken. Figure 7 represents the RDFs obtained via Fourier transformation of k^1 -weighted $\chi(k)$ for Se K-edge. The peak marked by the dotted line corresponds to Se–Ru and Se–Se interactions with the characteristic bond distances of $2.52 \pm 0.05 \text{ \AA}$ and $2.48 \pm 0.05 \text{ \AA}$, respectively. Hence, the EXAFS data confirm formation of Ru–Se and Se–Se bonds. It is remarkable that high quality of the fits can only be attained if Se–Se neighbors are considered. Short Se–Se distances are typical of Ru diselenide²⁴ and organometallic complexes containing RuSe_2 core.³⁴ Se–Ru and Se–Se distances are observed for all Ru_xSe_y samples examined in this work. It should be noted that although the corresponding

coordination numbers change from sample to sample (decreasing with the increase in the amount of Se), the ratio $N(\text{Ru})/N(\text{Se})$ in the first coordination shell is constant and equals 2.2 ± 0.2 . Along with the short Se–Se distance at $2.48 \pm 0.05 \text{ \AA}$, the longer ($\sim 3.36 \text{ \AA}$) distance characteristic of RuSe_2 structure is also observed but the corresponding coordination numbers are low. This points to the small size of Ru_xSe_y clusters (layers). Similar Se–Se distances are present in Se^0 ,^{36–38} so that one cannot exclude the presence of some amount of elementary Se in the samples. However, constant $N(\text{Ru})/N(\text{Se})$ ratio strongly suggests that both Se–Ru and Se–Se distances correspond to Ru selenide which local coordination is independent of the Se/Ru ratio.

Along with Se–Ru and Se–Se, shorter distances are observed; they give rise to peaks at short $R - \delta_i$ (see Figure 7, dashed line) and are attributed to Se–O bonds. As seen from Table 5, the Se–O distances obtained by fitting are close to those for bulk selenium oxides.^{39–41} However, the corresponding coordination numbers are greatly lowered as compared with those for the reference samples, and Se–Se distances at $3.1–3.2 \text{ \AA}$ (characteristic of Se–O–Se bridge bond) typical for bulk selenium oxides are not found. This testifies against formation of bulk Se oxides and proves that only surface oxidation of Se takes place. It is interesting that according to EXAFS Se–O coordination numbers grow with the increase of Se content in the samples, which is in conflict with the XPS results. This inconsistency is ascribed to the difference in the measurement conditions (cf. UHV for XPS and ambient conditions for EXAFS).

On the basis of the EXAFS data for the first coordination shell, the local arrangement of the clusters formed can be described as $\text{Ru}_{(2.25-1.4x)}\text{Se}_{(1.95-0.44x)}\text{O}_{(0.3+2x)}$ (where $x = \text{Se}/\text{Ru}$). As the Se/Ru ratio increases from 0.15 to 0.59, the amount of oxygen in the first coordination shell also increases. At higher Se/Ru = 1 no further increase in the O coordination is observed. We have recently performed in situ EXAFS studies which proved that polarization of the samples at 50 mV vs RHE reduces the amount of O in Se shell drastically and cancels the growth of the Se–O coordination numbers upon the increase of Se content.⁴² This will be discussed in detail in the forthcoming publication.

Although the exact structure and composition of Ru_xSe_y cannot be unambiguously corroborated from the experimental data due to the coexistence of Ru selenide clusters and metallic Ru, we would like to speculate on the tentative scenario for the interaction of Se with Ru. We suggest that Se is connected to two Ru and one Se ion forming a tetrahedral Ru_2Se_2 core which

TABLE 5: Distances (*R*) and Coordination Numbers (*N*) for Ru_xSe_y/C Samples (as calculated from Se K-edge EXAFS spectra) and for Reference Compounds^a

	Ru ₁ Se _{0.15} /C		Ru ₁ Se _{0.3} /C		Ru ₁ Se _{0.59} /C		Ru ₁ Se ₁ /C		SeO ₂ ³⁹		Se ₂ O ₅ ⁴¹		SeO ₃ ⁴⁰		RuSe ₂ ²⁴		Se ^{0.37}		Se ^{0.36}		Se ₆ ³⁸	
	<i>R</i> , Å	<i>N</i>	<i>R</i> , Å	<i>N</i>	<i>R</i> , Å	<i>N</i>	<i>R</i> , Å	<i>N</i>	<i>R</i> , Å	<i>N</i>	<i>R</i> , Å	<i>N</i>	<i>R</i> , Å	<i>N</i>	<i>R</i> , Å	<i>N</i>	<i>R</i> , Å	<i>N</i>	<i>R</i> , Å	<i>N</i>	<i>R</i> , Å	<i>N</i>
Se–O											1.57	1	1.55	1								
											1.62	1	1.56	1								
Se–O	1.57	0.2	1.56	0.3	1.56	0.5	1.56	0.5	1.62	1	1.69	1	1.75	1								
Se–O	1.77	0.4	1.75	0.6	1.76	1.0	1.76	1.0	1.79	2	1.73	1	1.80	1								
Se–Se	2.48	0.9	2.47	0.8	2.48	0.7	2.48	0.6	3.13	2	~3.22	1	3.13	2	2.45	1	2.39	2	2.38	2	2.37	2
Se–Ru	2.52	2.0	2.51	1.9	2.51	1.4	2.52	1.3							2.47	3						
Se–Se	3.37	0.4	3.38	0.3	3.38	0.2	3.39	0.2	3.88	4	3.87	1	4.32	5	3.36	6	3.10	4	3.43	4	3.43	2
											3.90	1	4.74								3.48	1

^a The values of Debye–Waller factors are fixed at 0.005 Å².

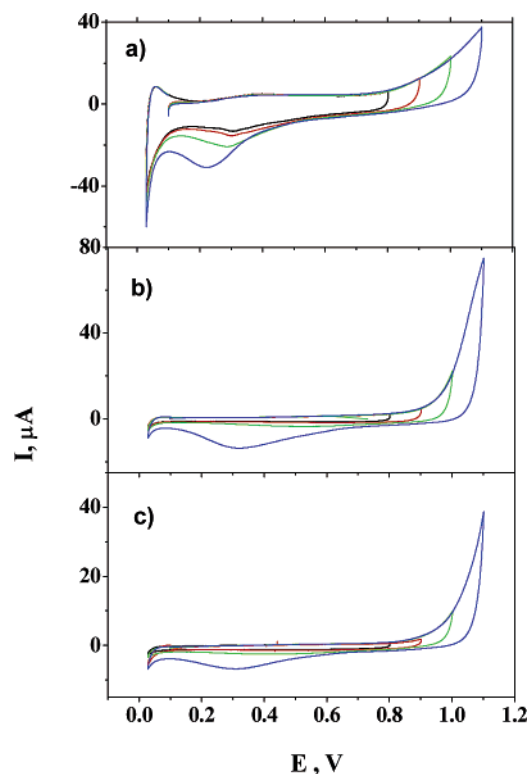


Figure 8. CVs with variable anodic limits for Ru/C (a), Ru₁Se_{0.15}/C (b), and Ru₁Se₁/C (c) in 0.1 M H₂SO₄ at 298 K. Scan rate 5 mV s^{−1}. Catalysts (3 × 10^{−5} g) were deposited on Au support. Note different scales in parts a–c.

is well-known from organometallic chemistry. Since samples are stored under the ambient atmosphere, oxygen is also coordinated to the clusters. Increase in the amount of Se in the samples is likely to result in the substitution of some Ru ions in the first shell of Se by Se ions. It is likely that the decrease of the amount of Ru in the Se surrounding will lead to the increase of Se susceptibility toward oxidation. Hence, the observed increase in the Se–O coordination numbers.

3.5. Electrochemical Properties. Figure 8a shows CVs of 20% Ru/Vulcan XC-72 in 0.1 M H₂SO₄. Similar anodic/cathodic peaks in the potential region from 0.03 to 0.17 V vs RHE were observed for Ru single crystals and were attributed to OH_{ads} formation/stripping.^{43–45} At more positive potentials various oxygen adlayers have been identified on the Ru(0001) single-crystal surface.⁴⁶ Surface oxide formation on Ru nanoparticles is likely to commence above 0.2 V. The cathodic broad counter peak between 0.2 and 0.4 V can be thus attributed to the surface oxide reduction. When the upper potential limit exceeds 0.8 V, the oxide reduction peak shifts negative, which suggests an increased irreversibility of the surface oxidation.

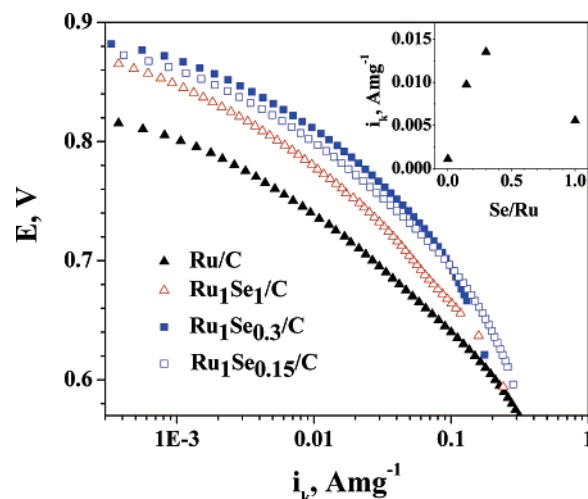


Figure 9. Mass transport corrected currents calculated from the positive sweeps of voltammograms acquired in still oxygen-saturated 0.1 M H₂SO₄ at 298 K with the scan rate 1 mV s^{−1} and referred to 1 mg of Ru. Catalysts (1.5 × 10^{−5} g) were mixed with Nafion (10 wt %) and deposited on the GC support. The inset shows the influence of Se/Ru ratio on the ORR kinetic current at 0.8 RHE.

Comparison of parts a, b, and c of Figure 8 reveals that modification of the surface of Ru nanoparticles with Se results in drastic changes in CVs (note different scales in Figure 8a–c): (i) the double layer splitting shrinks indicating the decrease of the interfacial capacitance; (ii) the peaks attributed to OH adsorption/desorption disappear; (iii) the anodic peak attributed to the build up of the Ru surface oxide disappears; (iv) the cathodic peak attributed to the oxide reduction diminishes and shifts to more positive potentials. Obviously, addition of Se to the catalysts inhibits electrochemical oxidation of Ru. This conclusion is in agreement with the literature data on Ru_xSe_y–(Mo₂) ORR catalysts.^{6,9,47} On the other hand, one may notice an appearance of significant anodic currents for Se-containing samples above ca. 0.9 V RHE. The anodic charge for Ru₁Se₁/C is not compensated by the cathodic counterpart and can be attributed to the dissolution of Se. This will be discussed in more detail in the forthcoming publication on the basis of in situ EXAFS data.⁴²

Figure 9 compares the kinetic currents *i_k* for the ORR of the pristine and Se-doped Ru/C samples. The voltammograms were acquired in still oxygen-saturated electrolyte. The currents were mass transport corrected assuming *i_k* = [*i*·*i_d*/(*i_d* − *i*)], where *i_d* stands for the diffusion-limited current. A detailed kinetic investigation of the ORR performed using a rotating disk electrode will be published elsewhere.⁴⁸ In agreement with the literature data, addition of Ru to Se considerably decreases the ORR overpotential. The higher the electrode potential, the higher the impact of Se on the ORR activity. At 0.8 V addition of Se

offers more than an order of magnitude increase in kinetic current. The dependence of the ORR activity on Se/Ru ratio is demonstrated in the inset in Figure 9. It is evident that relatively small amounts of Se (Se/Ru = 0.3) are needed in order to achieve a 10 times increase in the ORR activity. Considering the size of Ru nanoparticles, the apparent Se coverage (assuming one Se per one surface Ru atom) can be estimated as ca. 1 monolayer for the Ru₁Se_{0.3}/C sample. Further increase in Se loading results in a decrease of the ORR activity, which however still exceeds the catalytic activity of the Ru/C catalyst. Hence, encapsulation of Ru particles in Ru_xSe_y shells has a negative effect on the electrocatalytic activity.

Summary and Conclusions

The addition of SeO₂ to Ru nanoparticles supported on carbon followed by the reductive annealing results in the deposition of Se on Ru nanoparticles. Considering the size of Ru nanoparticles the apparent Se coverage (assuming one Se per one surface Ru atom) can be estimated as ca. 0.5 monolayer for Ru₁Se_{0.15}/C sample. However, this number can only serve as a rough estimate, since Se is not deposited in its elementary form but strongly interacts with Ru particles and forms Ru selenide on their surfaces. Interaction of Ru particles with Se results in significant attenuation of their size confirmed by XRD, TEM, and EXAFS. Formation of the chemical bond between Ru and Se is proven by the XPS and EXAFS data. At Se/Ru ≤ 0.59 HRTEM gives evidence for the formation of small <1 nm clusters on the surface of Ru particles which are attributed to Ru selenide. On the basis of the EXAFS data for the nearest neighbors, the core of these clusters can be described as Ru_(2.25–1.4x)Se_(1.95–0.44x)O_(0.3+2x) (where x = Se/Ru). At low Se content this roughly corresponds to Ru₂Se₂O_{0.5}. At high Se/Ru = 1, core-shell structures are observed comprising hexagonally packed Ru cores and Ru selenide shells, which adopt lamellar structure. The local coordination of Se in these shells is the same as that in the clusters formed at lower Se/Ru ratios. Despite the fact that the positions of the experimentally observed broad reflections in 2θ intervals from 28° to 38°, and from 48° to 56° agree well with the simulated XRD pattern for RuSe₂ with the crystal size 10 Å × 10 Å × 11.86 Å, we cannot unambiguously attribute Ru selenide formed upon the addition of Se to Ru/C to RuSe₂ with pyrite structure. The morphology of the particle shells is in disagreement with the cubic pyrite structure. It is likely that due to the size confinement, the surface Ru selenide formed in this work adopts a yet unknown structure. Strong interaction between Ru and Se not only results in the surface modification but also causes particle agglomeration. Recent data show that the latter can be minimized by optimization of the synthetic procedure.⁴⁹

Modification of Ru nanoparticles with Se strongly influences their susceptibility to oxidation: the higher the amount of Se, the lower the extent of Ru oxidation. This is confirmed by the physical techniques as well as by cyclic voltammetry. Transformation of the interfacial properties positively affects the electrocatalytic activity of Ru in the ORR. It is suggested that the increase in the ORR activity is related to the inhibition of Ru oxidation.

It is interesting to mention that Cao et al.⁵⁰ have found that surface modification of bulk polycrystalline Ru with Se does not lead to the comparable enhancement of the ORR activity. Considering the results of this work, we suggest that bonding between Ru and Se and formation of surface Ru selenide is essential for the ORR activity. On the other hand, according to the earlier publication, molecular oxygen binds to Ru centers.⁹

It is thus likely that formation of the surface compound strongly affects the electronic properties of Ru optimizing Ru–oxygen interactions and favoring the ORR. However, the selenide layer must be sufficiently thin and must not block the access of oxygen molecules to Ru centers. Obviously, this condition is not fulfilled for the samples with the high (1:1) Se content. In this context it is interesting to mention that being poisonous in high quantities, in small amounts Se in vivo acts as an antioxidant which delays the oxidation of polyunsaturated fatty acids and protects normal cell function by supporting the body's natural defenses and scavenging harmful free radicals.⁵¹ Intake of selenium greatly reduces occurrence of some cancers.

Acknowledgment. Financial support from BMBF under O2Red Network project (under Grant N°01SF0302) is gratefully appreciated. E.R.S. and K.N.L. greatly appreciate the technical assistance from Mrs. E. D. Pahomova.

References and Notes

- (1) Wasmus, S.; Küver, A. *J. Electroanal. Chem.* **1999**, *461*, 14.
- (2) *Handbook of Fuel Cells: Fundamentals, Technology and Applications*; Vielstich, W., Lamm, A., Gasteiger, H. A., Eds.; Wiley: Chichester, 2003; Vol. 2.
- (3) Alonso-Vante, N.; Giersig, M.; Tributsch, H. *J. Electrochem. Soc.* **1991**, *138*, 639.
- (4) Solorza-Feria, O.; Ellmer, K.; Giersig, M.; Alonso-Vante, N. *Electrochim. Acta* **1994**, *39*, 1647.
- (5) Alonso-Vante, N.; Solorza-Feria, O. *Electrochim. Acta* **1995**, *40*, 567.
- (6) Alonso-Vante, N. Chevrel phases and chalcogenides. In *Handbook of Fuel Cells. Fundamentals, Technology and Applications*; Vielstich, W., Lamm, A., Gasteiger, H. A., Eds.; Wiley: Chichester, 2003; p 534.
- (7) Schmidt, T. J.; Paulus, U. A.; Gasteiger, H. A.; Alonso-Vante, N.; Behm, R. J. *J. Electrochem. Soc.* **2000**, *147*, 2620.
- (8) Alonso-Vante, N.; Malakhov, I. V.; Nikitenko, S. G.; Savinova, E. R.; Kochubey, D. I. *Electrochim. Acta* **2002**, *47*, 3807.
- (9) Malakhov, I. V.; Nikitenko, S. G.; Savinova, E. R.; Kochubey, D. I.; Alonso-Vante, N. *J. Phys. Chem. B* **2002**, *106*, 1670.
- (10) Alonso-Vante, N.; Borthen, P.; Fieber-Erdmann, M.; Strehlow, H. H.; Holub-Krappe, E. *Electrochim. Acta* **2000**, *45*, 4227.
- (11) Dassenoy, F.; Vogel, W.; Alonso-Vante, N. *J. Phys. Chem. B* **2002**, *106*, 12152.
- (12) Le Rhun, V.; Alonso-Vante, N. *J. New Mater. Electrochem. Syst.* **2000**, *3*, 331.
- (13) Bron, M.; Bogdanoff, P.; Fiechter, S.; Hilgendorff, M.; Radnik, J.; Dorbandt, I.; Schulenburg, H.; Tributsch, H. *J. Electroanal. Chem.* **2001**, *517*, 85.
- (14) Hilgendorff, M.; Diesner, K.; Schulenburg, H.; Bogdanoff, P.; Bron, M.; Fiechter, S. *J. New Mater. Electrochem. Syst.* **2002**, *5*, 71.
- (15) Bönemann, H.; Endruschat, U.; Hormes, J.; Köhl, G.; Kruse, S.; Modrow, H.; Mörtel, R.; Nagabhushana, K. S. *Fuel Cells* **2004**, *4*, 1.
- (16) Vishnevskii, A. L.; Molchanov, V. V.; Kriger, T. A.; Plyasova, L. M. In *Book of Abstracts*, International Conference On Powder Diffraction and Crystal Chemistry, St. Petersburg, 1994; p 206.
- (17) <http://sun.phy.cuhk.edu.hk/~surface/XPSPEAK/XPSPEAKusers-guide.doc>.
- (18) Kochubey, D. I. *EXAFS spectroscopy of catalysts*, Novosibirsk, Nauka, 1992 (in Russian).
- (19) Koningsberger, D. C.; Mojet, B. L.; Dorssena, G. E. v.; Ramaker, D. E. *Top. Catal.* **2000**, *10*, 143.
- (20) Klementiev, K. V. *J. Phys. D: Appl. Phys.* **2001**, *34*, 209.
- (21) Klementiev, K. V. *code VIPER for Windows, freeware: www.desy.de/~klmn/viper.html*.
- (22) Binsted, N.; Campbell, J. V.; Gurman, S. J.; Stephenson, P. C. SERC Daresbury Laboratory EXCURV92 program, 1991.
- (23) Cauzzi, D.; Graiff, C.; Pattacini, R.; Predieri, G.; Tiripicchio, A. J. *Braz. Chem. Soc.* **2003**, *14*, 908.
- (24) ICSD Collection Code 68473, I. d., 1997.
- (25) Dey, S.; Jain, V. K. *Platinum Met. Rev.* **2004**, *48*, 16.
- (26) Tsybulya, S. V.; Cherepanova, S. V.; G. N., K., *Diffraction Analysis of the Microstructure of Materials*; Springer: Berlin, 2004; p 549.
- (27) Jacob, T. Unpublished results.
- (28) Yin, Y.; Rioux, R. M.; Erdonmez, C. K.; Hughes, S.; Somorjai, G. A.; Alivisatos, A. P. *Science* **2004**, *304*, 711.
- (29) Kinoshita, K. *Carbon. Electrochemical and Physicochemical Properties*; John Wiley & Sons: New York, 1988; p 533.

- (30) Moulder, J. F.; Stickle, W. F.; Sobol, P. E.; Bomben, K. D., *Handbook of X-ray Photoelectron Spectroscopy*; Perkin-Elmer: Eden Prairie, MN, 1992; p 261.
- (31) Alonso-Vante, N.; Cattarin, S.; Musiani, M. *J. Electroanal. Chem.* **2000**, 481, 200.
- (32) ICSD Collection Code 43710, I. d., 1997.
- (33) ICSD Collection Code 23961, I. d., 1997.
- (34) Killops, S. D.; Knox, S. A. R. *J. Chem. Soc., Dalton Trans.* **1978**, 1260.
- (35) Johnson, B. F. G.; Lewis, J.; Lodge, P. G.; Raithby, P. R.; Henrick, K.; McPartlin, M. *J. Chem. Soc., Chem. Commun.* **1979**, 16, 719.
- (36) ICSD Collection Code 40018, I. d., 1997.
- (37) ICSD Collection Code 200687, I. d., 1997.
- (38) ICSD Collection Code 86375, I. d., 1997.
- (39) ICSD Collection Code 72366, I. d., 1997.
- (40) ICSD Collection Code 18180, I. d., 1997.
- (41) ICSD Collection Code 10471, I. d., 1997.
- (42) Kriventsov, V. V.; Loponov, K. N.; Kochubey, D. I.; Savinova, E. R. Unpublished results.
- (43) El-Aziz, A. M.; Kibler, L. A. *Electrochem. Commun.* **2002**, 4, 866.
- (44) Marinkovic, N. S.; Wang, J. X.; Zajonz, H.; Adzic, R. R. *J. Electroanal. Chem.* **2001**, 500, 388.
- (45) Brankovic, S. R.; Wang, J. X.; Zhu, Y.; Sabatini, R.; McBreen, J.; Adzic, R. R. *J. Electroanal. Chem.* **2002**, 524, 231.
- (46) Zei, M. S.; Ertl, G. *Phys. Chem. Chem. Phys.* **2000**, 2, 3855.
- (47) Bron, M.; Bogdanoff, P.; Fiechter, S.; Dorbandt, I.; Hilgendorff, M.; Schulenburg, H.; Tributsch, H. *J. Electroanal. Chem.* **2001**, 500, 510.
- (48) Loponov, K. N.; Savinova, E. R. Unpublished data.
- (49) Nagabhushana, K. Unpublished data.
- (50) Cao, D.; Wieckowski, A.; Inukai, J.; Alonso-Vante, N. In press.
- (51) Harrison, P. R.; Lanfear, J.; Wu, L. *Biomed. Environ. Sci.* **1997**, 10, 235.
- (52) ICSD Collection Code 33799, I. d., 1997.